Volume 19
Number 2
27 January 2026
Pages 401–732

Energy & Environmental Science

rsc.li/ees

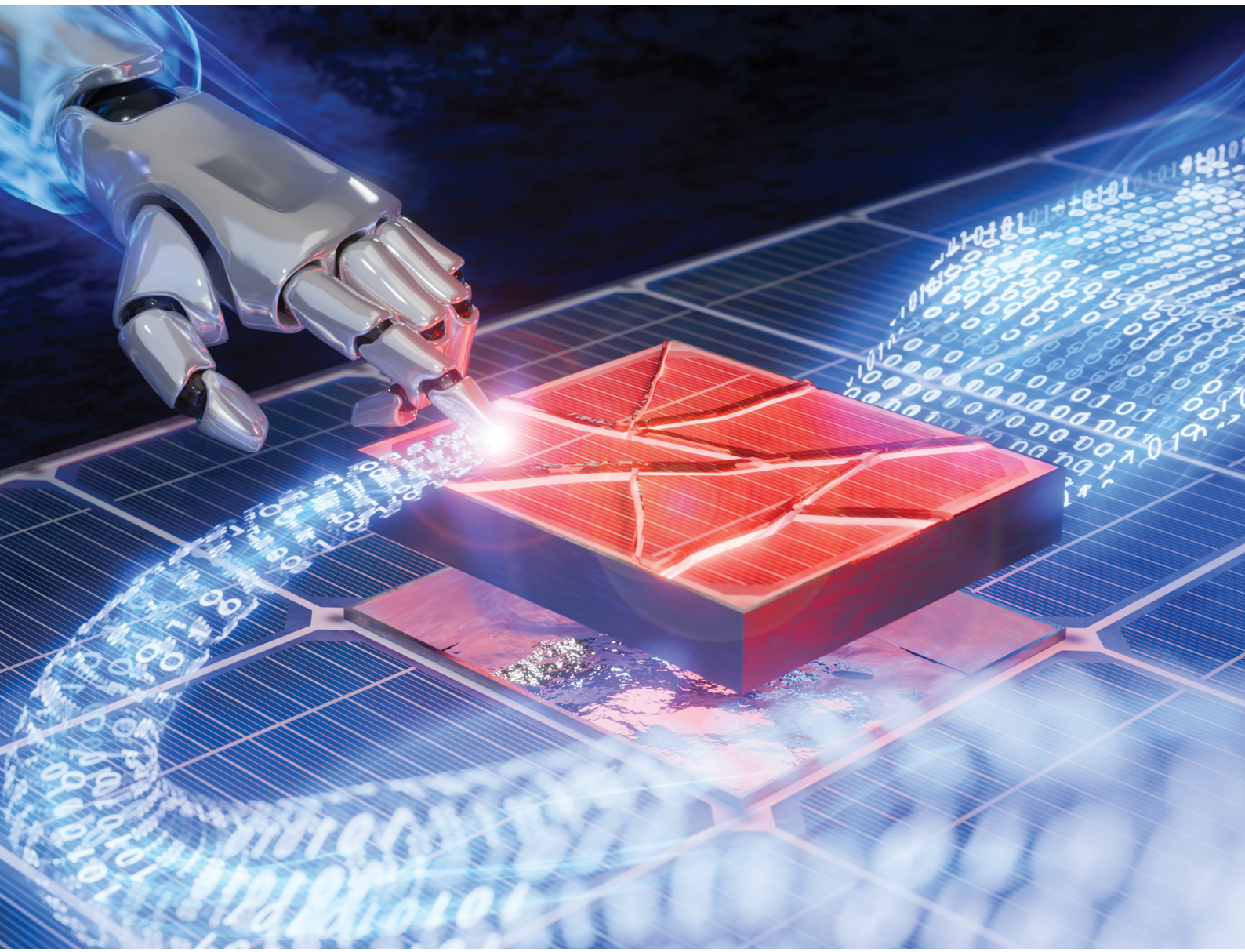

ISSN 1754-5706

ROYAL SOCIETY OF CHEMISTRY

PAPER

Kaiwen Sun, Xiaojing Hao *et al.*

Unsupervised and few-shot segmentation in photovoltaic electroluminescence images for defect detection *via* a novel enhanced iterative autoencoder with simple implementation

Energy & Environmental Science

ROYAL SOCIETY OF CHEMISTRY

PAPER

View Article Online
View Journal | View Issue

Open Access Article. Published on 26 noiembrie 2025. Downloaded on 13.02.2026 21:51:31.
This article is licensed under a Creative Commons Attribution-NonCommercial 3.0 Unported Licence.

Check for updates

Cite this: *Energy Environ. Sci.*, 2026, **19**, 513

Unsupervised and few-shot segmentation in photovoltaic electroluminescence images for defect detection *via* a novel enhanced iterative autoencoder with simple implementation

Ye Lin, †[abe] Pingyang Sun, †*[c] Rongcheng Wu, †[ab] Shu Geng,[d] Man Lung Yiu,[e] Zhidong Li,[b] Fang Chen,[b] Yu Gao,[a] Mingzhe Wang,*[f] Kaiwen Sun *[c] and Xiaojing Hao*[c]

Received 27th August 2025,
Accepted 24th November 2025

DOI: 10.1039/d5ee05042a

rsc.li/ees

Photovoltaic electroluminescence (PVEL) imaging captures material-level degradation in PV modules and offers high-resolution input for machine learning (ML) models to perform automated fault detection and health evaluation, reducing reliance on manual inspection. It is expected to have a simple and efficient defect detection ML model to achieve accurate segmentation for the fine-featured identification of defects in fabricated PV modules. This study proposes a novel enhanced iterative autoencoder (EI-AE), a completely new model that differs fundamentally from existing approaches which rely directly on classical ML models for defect detection. The proposed EI-AE, which for the first time introduces an iterative mechanism into the traditional AE framework, features a simple yet effective architecture and achieves accurate unsupervised pixel-level segmentation of all defect types using only normal PVEL images. In addition, few-shot learning can be realized by extending the unsupervised EI-AE with a small number of annotated masks, allowing more detailed functional defect detection while mitigating background interference. Theoretical proof demonstrates the benefits of the proposed EI-AE in improving defect detection compared to the conventional AE. Experimental results further validate its superiority, showing consistently better performance across multiple pixel-level metrics and outperforming both widely used unsupervised and few-shot baseline approaches.

Broader context

Photovoltaic (PV) systems are expanding rapidly worldwide, making reliable and cost-effective maintenance increasingly important. PV electroluminescence (PVEL) imaging provides high-resolution visual data that reveal material-level degradation in PV modules. These images are particularly valuable for machine learning (ML)-based automated fault detection and health assessment, reducing reliance on manual inspection. Achieving accurate segmentation of minute defects in fabricated PV modules requires a defect detection model that is both simple and efficient. This study presents an enhanced iterative autoencoder (EI-AE), a fundamentally new model that, for the first time, incorporates an iterative mechanism into the conventional AE framework. Unlike existing methods that rely directly on classical ML architectures, EI-AE features a simple yet effective design capable of performing fully unsupervised, pixel-level segmentation of all defect types using only normal PVEL images. Furthermore, by extending the unsupervised EI-AE with a small set of annotated masks, the framework supports few-shot learning, enabling more detailed functional defect identification while suppressing background interference.

[a] *Molly Wardaguga Institute for First Nations Birth Rights, Faculty of Health, Charles Darwin University, Brisbane, QLD, 4000, Australia. E-mail: yu.gao@cdu.edu.au*
[b] *The Data Science Institute, University of Technology Sydney, Sydney, NSW, 2007, Australia. E-mail: rongcheng.wu@student.uts.edu.au*
[c] *School of Photovoltaic and Renewable Energy Engineering, University of New South Wales, Sydney, NSW, 2052, Australia. E-mail: xj.hao@unsw.edu.au*
[d] *School of Chemical Engineering and Australian Centre for Nanomedicine (ACN), The University of New South Wales, Sydney, NSW, 2052, Australia. E-mail: shu.geng@unsw.edu.au*
[e] *Department of Computing, The Hong Kong Polytechnic University, Hong Kong, 999077, China. E-mail: csmlyiu@polyu.edu.hk*
[f] *School of Computer Science and Technology, Xidian University, Xi'an, Shaanxi, 710126, China. E-mail: wangmingzhe@xidian.edu.cn*
† Y. Lin, P. Sun and R. Wu contributed equally to this work.

Open Access Article. Published on 26 noiembrie 2025. Downloaded on 13.02.2026 21:51:31.
This article is licensed under a Creative Commons Attribution-NonCommercial 3.0 Unported Licence.

1 Introduction

Photovoltaic electroluminescence (PVEL) imaging is a non-destructive technique for assessing PV module quality,[1] revealing microscopic defects such as microcracks, inactive areas, broken fingers, shunts, and soldering issues that are often undetectable by visual inspection. It enables early detection of hidden defects during manufacturing, installation, or operation, supporting quality assurance, performance prediction, and reliability assessment.[2] Due to the large volume and complexity of PVEL data, manual inspection is inefficient and error-prone, making automated defect detection algorithms[3] essential for large-scale, reliable, and real-time assessment.[4]

Machine learning (ML) can automatically detect defects in PVEL images by learning complex patterns,[4,5] outperforming conventional image processing.[6,7] While most ML methods address defect detection,[8–13] advanced approaches perform defect segmentation to localize defective regions, as illustrated in Fig. 1. ML has been applied to (i) correlating defects with power output,[14,15] (ii) detecting defects before lamination,[16,17] (iii) enhancing image quality,[18,19] and (iv) identifying defects in assembled modules.[8,20–22] PVEL images of assembled PV modules contain rich spatial and intensity information that reflects subtle material and manufacturing defects, making them highly suitable for automated analysis.[8] To identify defects in PVEL images of finished PV modules, three types of defect detection ML approaches can be utilized: (i) image-level binary and multi-class classification, (ii) bounding box-based object localization, and (iii) segmentation. This work focuses on the defect identification of fabricated PV modules, and adopts segmentation[23] for pixel-level localization of complex defects to support automated EL image inspection.

Although image-level binary/multi-class classification is the most basic ML method for EL image defect detection, it assumes that all defect categories are fully defined and mutually exclusive. Convolutional neural networks (CNNs) dominate both tasks,[8–10] employing architectures such as VGG16,[11–13] high-resolution network (HRNet),[9,10,24] and the combination of ResNet152, Xception, and coordinate attention (CA).[25] Feature enhancement and model compression are achieved *via* the incorporation of histogram of oriented gradients (HoG)[12] and knowledge distillation[13] into VGG16. The current multi-class classification efforts mainly rely on CNN,[20,26–36] support vector machine (SVM),[26,30] and random forest (RF).[30,37] In addition, transfer learning with compact architectures has been adopted to utilize pre-trained features,[29] while architectural combinations[33] and particle swarm optimization (PSO)[35] further enhance accuracy and reduce model complexity. Other approaches include modified VGG19,[28] unsupervised clustering,[27] generative adversarial network (GAN)-based augmentation,[32] fuzzy logic integration,[34] and defect localization by YOLO.[36] Unlike classification, bounding box methods detect multiple defects per module. Fusion of Faster regions with CNN features (R-CNN) and region-based fully convolutional network (R-FCN) outputs based on intersection over union (IoU) consistency improves accuracy and reduces false detections.[21] Incorporating a complementary attention network (CAN) into a Faster R-CNN's region proposal network further enhances defect extraction.[5] Mask R-CNN with a ResNet-101-FPN backbone detects fourteen defect types.[38] However, the classification and bounding box-based defect localization tasks are often limited in providing detailed spatial information, which segmentation can overcome by delivering pixel-level defect mapping for precise assessment.

For the segmentation task, two paradigms can be utilized: (1) approaches that use a separate feature extractor followed by a segmentation procedure,[22,39–41] and (2) end-to-end segmentation networks.[42–46] Classification networks, such as ResNet18[40] and ResNet50,[22,41] can serve as backbone feature extractors, with their outputs passed to a segmentation head, such as autoencoder (AE)[39] and DeepLabv3,[41] for pixel-wise prediction. Instead of performing explicit segmentation, a ResNet-50 trained for classification is used to generate intermediate activation maps,[22] whose spatial responses are interpreted as segmentation.

End-to-end segmentation networks are task-optimized for accurate, dense defect detection of PVEL images. A GAN is used to produce more realistic reconstructions of normal samples through adversarial training.[42] However, GANs often suffer from training instability and typically require larger datasets, which limit their practicality in industrial settings. Different encoder–decoder NN architectures are also explored in PVEL image defect detection, including standard U-Net,[44,46] U-Net with an attention mechanism,[43] PSPNet[46] and DeepLabv3+.[46] Multiple combinations of encoder and decoder networks are explored,[45] which are Mobile-net, ResNet, VGG-net, and U-net

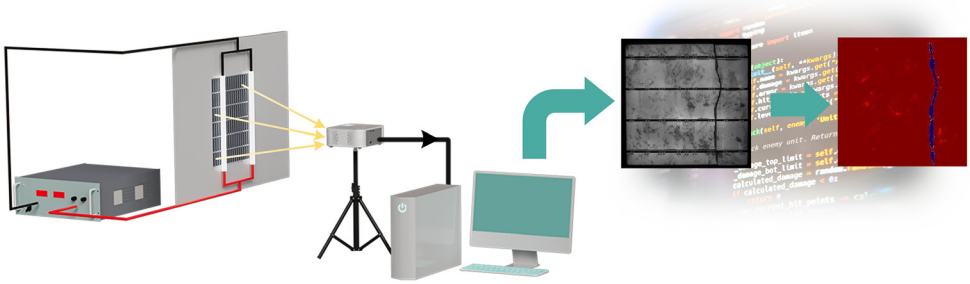

Fig. 1 PVEL image acquisition and machine learning-based defect segmentation.

Open Access Article. Published on 26 noiembrie 2025. Downloaded on 13.02.2026 21:51:31.
This article is licensed under a Creative Commons Attribution-NonCommercial 3.0 Unported Licence.

for the encoder part, while U-net, FCN-net, PSP-net, and SegNet for the decoder part. In addition, wavelet analysis is used to handle non-stationary textures in the segmentation of PVEL images,[47] while K-Net has been used as a baseline method in segmentation tasks.[48]

Nevertheless, the current studies on defect detection of PVEL images using end-to-end segmentation networks are still in the stage of direct use of classical NN models or their simple combinations. These approaches often lack adaptability to subtle or complex defect patterns, especially in cases involving irregular morphology or background interference. To address this limitation, a novel enhanced iterative autoencoder (EI-AE) is proposed in this study to achieve simple and accurate unsupervised defect segmentation of PVEL images using only normal samples during training. The proposed EI-AE utilizes U-Net[49] as encoder and decoder blocks, while iterative operations[50] are implemented in each encoder and decoder to significantly (i) expand function space constraints (enhancing the ability to generalize from normal PVEL image patterns), (ii) prevent defect memorization (avoiding the model from incorrectly learning and reconstructing latent defects in normal-looking PVEL images), and (iii) improve multi-scale information representation (accurately detecting defects of varying sizes in PVEL images). In addition, by incorporating a multi-image fusion structure, the proposed EI-AE can be adapted to detect more specific defects using a few-shot approach with only a limited number of annotated functional defect masks.

2 Description of datasets

In this work, we use the photovoltaic electroluminescence anomaly detection (PVEL-AD) dataset,[51] which comprises 36 543 near-infrared images (11 353 good images) of solar cells featuring various internal defects and heterogeneous backgrounds. The dataset includes one defect-free category and 12 distinct defect types, namely black cores, corner defects, cracks (non-star), finger interruptions, fragments, horizontal dislocations, printing errors, scratches, short-circuit defects, star cracks, thick lines, and vertical dislocations (two images of each category are shown in Fig. 2). The PVEL-AD dataset, with its long-tail distribution of defect types, provides a challenging while realistic benchmark for evaluating unsupervised and few-shot learning approaches. It is particularly well-suited for testing models (*e.g.* the proposed EI-AE), which performs segmentation using only normal samples, and can be extended with limited annotations to detect rare functional defects, addressing the annotation bottleneck in practical PV quality inspection.

Furthermore, to evaluate the segmentation performance under different settings of our proposed EI-AE, we manually annotated two types of segmentation masks (Mask A and Mask B) based on this dataset. All defects are captured in Mask A without explicitly defining the defect categories, while four specific defect types are annotated in Mask B. These additional annotations allow a more comprehensive assessment of segmentation accuracy and robustness.

2.1 All defect masks (Mask A)

In this setting, 30 masks are labelled for all observed defects, encompassing both functional and non-functional defects (18 images are shown in Fig. 3, while others are put in SI-S2). This comprehensive annotation strategy serves two main purposes. First, by including every visible defect, regardless of its specific impact on solar cell performance, we ensure that the

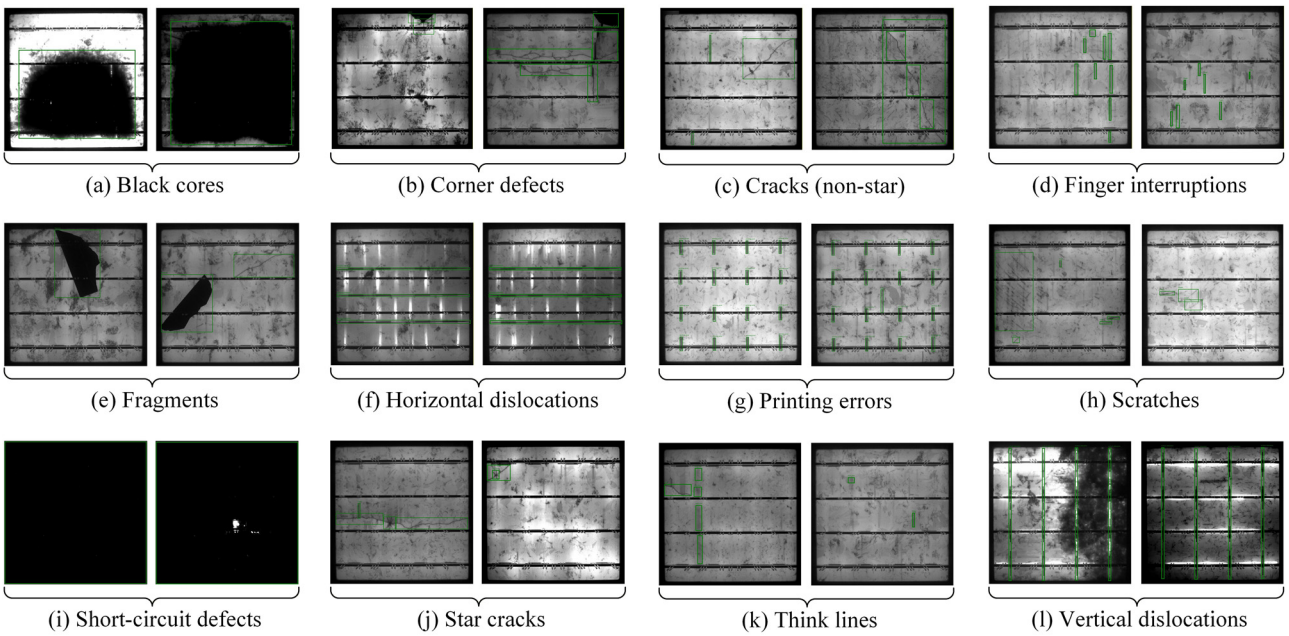

Fig. 2 Defect categories in the used PVEL-AD dataset: (a) black cores, (b) corner defects, (c) cracks (non-star), (d) finger interruptions, (e) fragments, (f) horizontal dislocations, (g) printing errors, (h) scratches, (i) short-circuit defects, (j) star cracks, (k) think lines, and (l) vertical dislocations.

Open Access Article. Published on 26 noiembrie 2025. Downloaded on 13.02.2026 21:51:31.
This article is licensed under a Creative Commons Attribution-NonCommercial 3.0 Unported Licence.

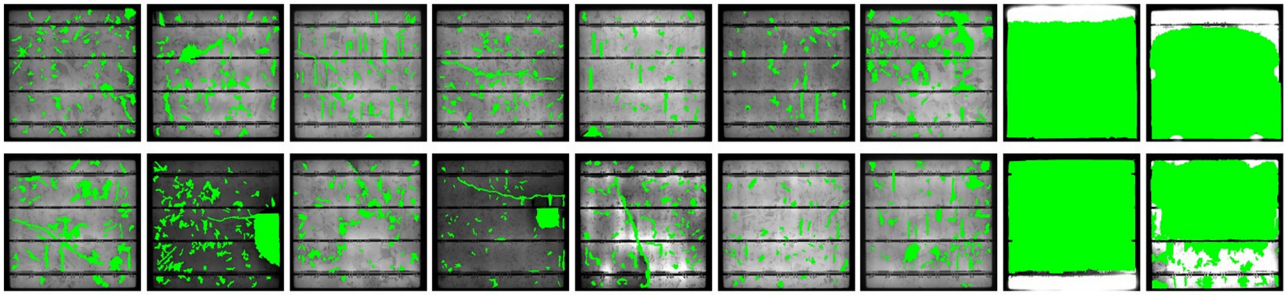

Fig. 3 All defect masks by manual annotation (Mask A).

segmentation model learns to detect a broad range of defect patterns. This coverage is especially relevant in real-world manufacturing contexts, where even minor or cosmetic defects (*e.g.*, scratches or tiny surface inconsistencies) may indicate underlying process issues. Second, the inclusive nature of this mask annotation provides a more holistic evaluation of a model's capacity to identify and localize any deviation from the nominal appearance. Consequently, the "All defects" mask allows for a thorough assessment of segmentation performance, highlighting the robustness of the proposed EI-AE in scenarios where defect types or severities vary widely.

2.2 Functional defect masks (Mask B)

In this setting, only defects that directly impact device performance are considered. Specifically, we use the bounding boxes provided by the PVEL-AD dataset to manually annotate high-resolution 438 masks within the testing set, targeting only functional defects. Although the PVEL-AD dataset[51] contains 12 types of defects, four major categories, including cracks (non-star), finger interruptions, scratches, and star cracks, are utilized and manually annotated in this study to demonstrate the effectiveness of the proposed EI-AE. In addition, three representative images from each annotated category are shown in Fig. 4, while the remaining annotated images are provided in SI-S3.

By refining the coarse bounding-box labels into pixel-precise segmentations, this annotation process ensures that our evaluations concentrate on those defects most critical to PV module reliability. Consequently, this approach enables an in-depth assessment of model performance in detecting and characterizing functionally significant defects, thereby facilitating more targeted strategies for quality control in smart manufacturing processes.

3 Proposed enhanced iterative autoencoder (EI-AE)

In this study, we propose a novel EI-AE unsupervised learning method for simple defect detection of PVEL images. The space of the PVEL input image can be expressed as $\mathscr{I} \subset \mathbb{R}^{h\times w\times c}$, where h, w, and c indicate the height, width, and number of channels, respectively. For the defect detection task, a training set $\mathscr{X}_{\text{train}}$ includes i normal EL images without abnormalities, while a test set $\mathscr{X}_{\text{test}}$ consists of t defective EL images, where $\mathscr{X}_{\text{train}} = \{\boldsymbol{x}_1,\boldsymbol{x}_2,\ldots,\boldsymbol{x}_i\}$, $\mathscr{X}_{\text{test}} = \{\boldsymbol{x}_1,\boldsymbol{x}_2,\ldots,\boldsymbol{x}_t\}$, and $\boldsymbol{x} \in \mathscr{I}$. The learning objective aims to develop a model capable of performing pixel-level segmentation to detect defective regions within test images $\mathscr{X}_{\text{test}}$.

3.1 Conventional autoencoder (AE)

Since the focus of this study is on 2D PVEL images, a traditional widely used convolutional AE for defect detection is first introduced in this section,[52,53] following with its challenge explanations in high-precision defect identification.

A convolutional AE is trained to minimize the reconstruction error $L_{\text{recon.}}$ on normal samples as:

$$L_{\text{recon.}} = \frac{1}{n}\sum_{i=1}^{n} \|\boldsymbol{x}_i - \tilde{\boldsymbol{x}}_i\|_p, \tag{1}$$

where n is the number of samples, $\|\cdot\|_p$ refers to the ℓ_p norm (typically $p = 1$, Manhattan norm or $p = 2$, Euclidean norm), and $\tilde{\boldsymbol{x}}_i$ denotes the reconstruction of the input image $\boldsymbol{x}_i$, expressed as:

$$\tilde{\boldsymbol{x}}_i = f_{\text{D}}(f_{\text{E}}(\boldsymbol{x}_i)), \tag{2}$$

where f_{D} is the encoder network ($\mathscr{I} \rightarrow \mathscr{Z}$) that processes the input image to obtain a latent representation $\mathscr{Z}$ ($\mathscr{Z} \subset \mathbb{R}^{h'\times w'\times c'}$, $h' < h$, $w' < w$, $c' \geq c$); f_{E} is the decoder network ($\mathscr{Z} \rightarrow \mathscr{I}$), which takes the latent representation Z produced by the encoder and reconstructs the input image. A deep convolutional AE with depth N can be represented as:

$$F_{\text{AE}}(\boldsymbol{x}) = f_{\text{D}_1}(f_{\text{D}_2}(\ldots f_{\text{D}_N}(f_{\text{E}_N}(\ldots f_{\text{E}_2}(f_{\text{E}_1}(\boldsymbol{x}))))))). \tag{3}$$

Moreover, the parameters of each encoder and decoder block are given by $\left\{\xi_{f_{\text{E}_1}}, \xi_{f_{\text{E}_2}}, \ldots, \xi_{f_{\text{E}_N}}\right\}$ and $\left\{\xi_{f_{\text{D}_1}}, \xi_{f_{\text{D}_2}}, \ldots, \xi_{f_{\text{D}_N}}\right\}$, respectively.

However, traditional AEs face several critical limitations when applied to industrial PVEL image defect detection:

(1) With a limited number of normal EL images, the AE is prone to overfitting, resulting in poor generalization.[54] Although the training objective minimizes the reconstruction loss as eqn (1), the network will memorize training examples when the training set $\mathscr{X}_{\text{train}}$ is small:

$$f_{\text{D}}(f_{\text{E}}(\boldsymbol{x}_i)) \approx \boldsymbol{x}_i, \forall \boldsymbol{x}_i \in \mathscr{X}_{\text{train}}. \tag{4}$$

Open Access Article. Published on 26 noiembrie 2025. Downloaded on 13.02.2026 21:51:31.
This article is licensed under a Creative Commons Attribution-NonCommercial 3.0 Unported Licence.

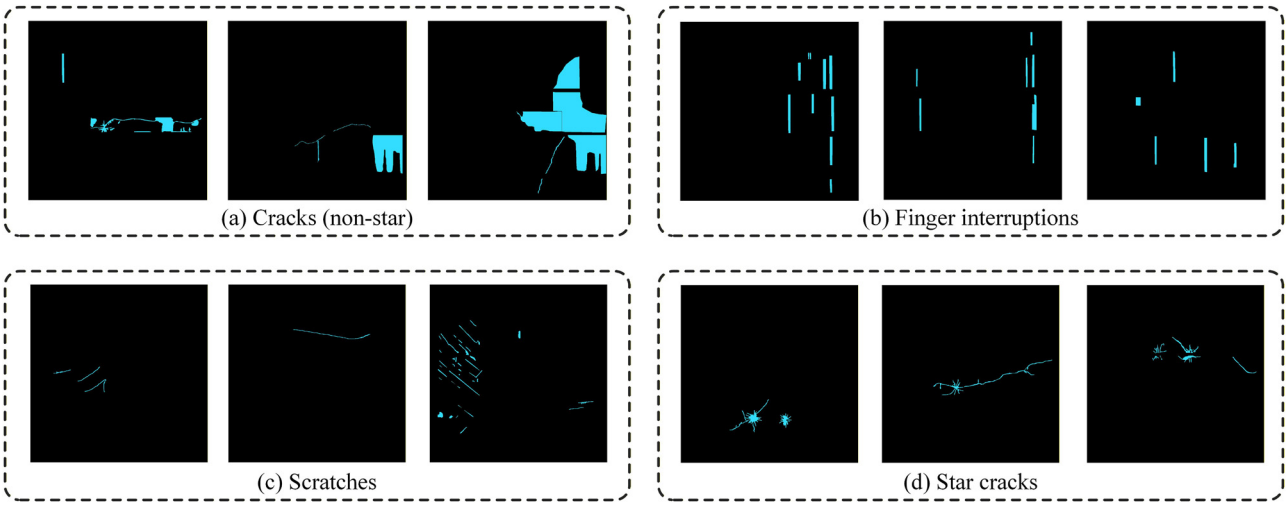

Fig. 4 Functional defect masks by manual annotation (Mask B): (a) cracks (non-star), (b) finger interruptions, (c) scratches, and (d) star cracks.

Since anomalies are absent in training, the model fails to generalize to unseen test samples $\mathscr{X}_{\text{test}} \notin \mathscr{X}_{\text{train}}$, making it unreliable for defect detection.

(2) When a high representation capacity is present in the latent space, the AE reconstructs both normal and defective samples accurately, making defect detection ineffective.[55] If the encoder f_{E} maps inputs to a high-capacity latent space $\mathscr{Z}$, then for any input $\boldsymbol{x}$, an expressive decoder can reconstruct it perfectly:

$$\boldsymbol{z}_i = f_{\text{E}}(\boldsymbol{x}_i),\ \boldsymbol{x}_i \approx f_{\text{D}}(\boldsymbol{z}_i), \tag{5}$$

Since defective data points $\boldsymbol{x}_{\text{anom}}$, are also mapped to similar latent representations, their reconstructions remain accurate:

$$\|\boldsymbol{x}_{\text{anom}} - f_{\text{D}}(f_{\text{E}}(\boldsymbol{x}_{\text{anom}}))\|_p \approx 0 \tag{6}$$

This contradicts the assumption that anomalies should have high reconstruction errors and thus reduces the effectiveness of defect detection.

(3) A standard AE reconstructs anomalies in a single resolution scale, lacking multi-scale feature extraction, which limits their ability to differentiate complex anomalies from normal variations.[56,57] The single encoding-decoding operation is expressed as:

$$\hat{\boldsymbol{x}}_i = f_{\text{D}}(f_{\text{E}}(\boldsymbol{x}_i)). \tag{7}$$

resulting in a failure in capturing hierarchical features. Since normal variations can exist at multiple scales (*e.g.*, subtle texture differences, cell pattern shifts, and illumination changes in PVEL images), the single-pass AE may fail to distinguish them from true anomalies, leading to misclassifications in anomalies.

3.2 Enhanced iterative autoencoder (EI-AE)

To address the potential issues of the conventional AE in the defect detection of PVEL images discussed in Section 3.1, this study proposes a novel EI-AE (Fig. 5) that utilizes iterative computation to achieve multi-step compression and reconstruction, improving parameter sharing and network representation capabilities. To be specific, the proposed EI-AE consists of two key stages: (i) a iterative compression encoder, and (ii) an iterative reconstruction decoder. These components jointly enhance function space constraints, prevent defect memorization, and improve multi-scale information representation, outperforming the conventional AE. This section presents the network architecture description of the proposed EI-AE, along with a detailed explanation of its improvements.

3.2.1 Iterative compression stage. The iterative compression stage, illustrated in the purple box of Fig. 5, reduces the resolution of the input PVEL image stepwise through $\mathscr{N}$ iterative iterations, while 5 iterations are used in this model.

A modified U-Net is implemented as an encoder in the compression stage by replacing the output layer of the standard U-Net with a convolutional layer with kernel size 2 and stride 2, so that the spatial dimensions (height and width) of the original input are reduced by half. This process is similar to the encoder in a standard AE, where the input is compressed in the compression layer.

However, unlike a standard AE, our approach employs a modified U-Net (U-Net-E) that iteratively refines the encoding process through $\mathscr{N}$ self-iterations within the encoder, continuously compressing the input into a lower-dimensional representation while sharing a common encoder f_{E} with parameters $\xi_{f_{\text{E}}}$:

$$\boldsymbol{S}_{\text{ItC}}^{(j)} = f_{\text{E}}(\boldsymbol{S}_{\text{ItC}}^{(j-1)};\xi_{f_{\text{E}}}),\ j \in \{1,2,3,\ldots,\mathscr{N}\}, \tag{8}$$

where $\boldsymbol{S}_{\text{ItC}}^{(0)} = \boldsymbol{x}$ indicates the original input image, and the spatial dimensions are reduced in each iteration. The shared encoder $f_{\text{E}}: \mathcal{I}_{j-1} \rightarrow \mathcal{I}_j$ transforms the input from one resolution level to a lower one, where $\mathcal{I}_i \subset \mathbb{R}^{h/2^j \times w/2^j \times c}$. The compression depth is limited to a maximum of $\mathscr{N} = 5$ for 1024×1024 input images, as further downsampling leads to excessively small feature maps and prevents the model from functioning.

Open Access Article. Published on 26 noiembrie 2025. Downloaded on 13.02.2026 21:51:31.
This article is licensed under a Creative Commons Attribution-NonCommercial 3.0 Unported Licence.

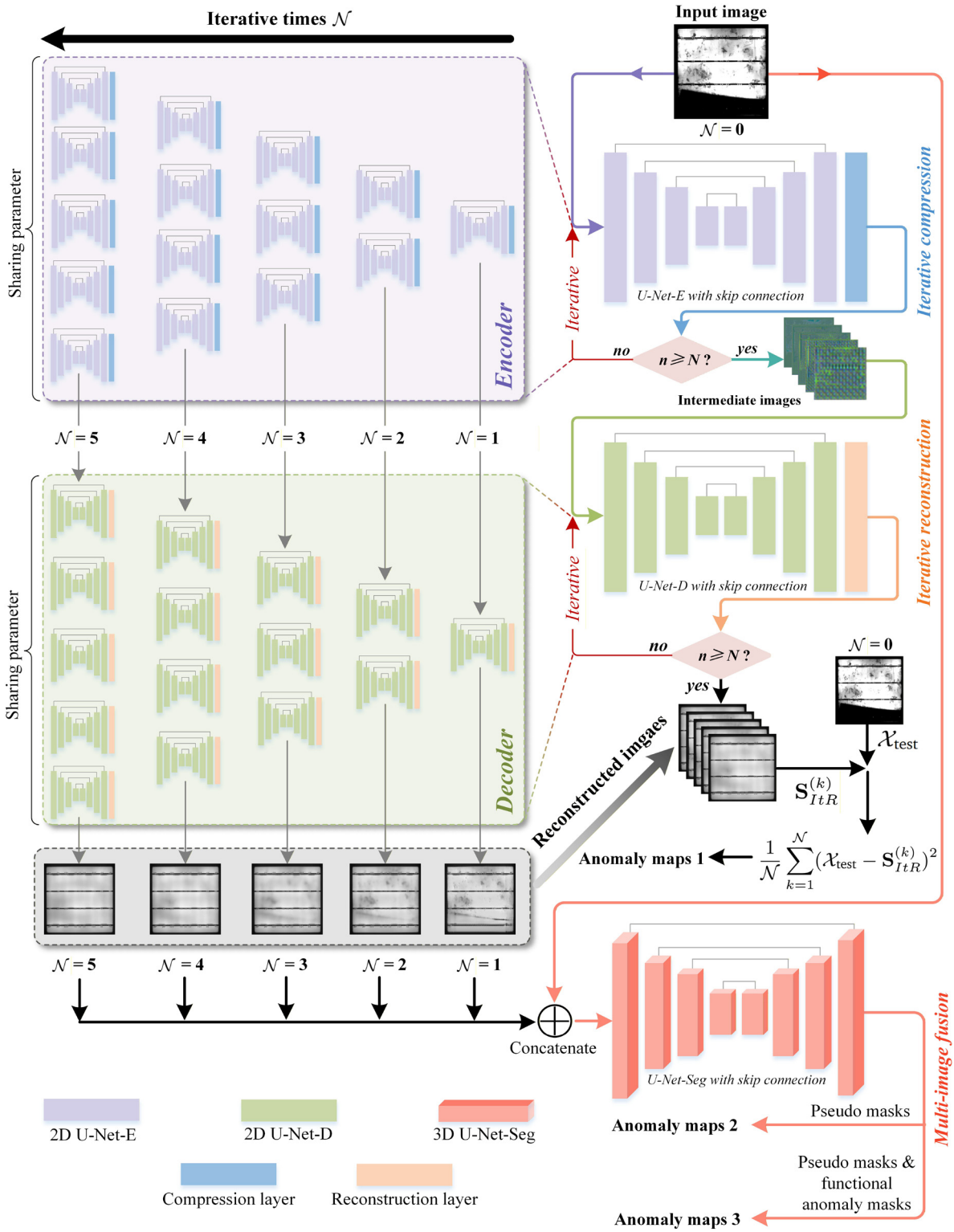

Fig. 5 Network framework of the proposed EI-AE for the defect detection of PVEL images.

3.2.2 Iterative reconstruction stage. The green-filled box of Fig. 5 shows the iterative reconstruction stage, which starts from the most compressed representation $\boldsymbol{S}_{\text{ItC}}^{(\mathcal{N})}$ in the iterative compression stage. Similar to the U-Net-E in the encoder, we also modify a standard U-Net to a new U-Net (U-Net-D) by replacing the output layer with a transposed convolution (deconvolution) layer with a kernel size of 2 and a stride of 2, upsampling the low-dimensional features back to the original input size.

Multiple self-iterations are performed in the new decoder to progressively upsample the low-dimensional features into

This journal is © The Royal Society of Chemistry 2026

Open Access Article. Published on 26 noiembrie 2025. Downloaded on 13.02.2026 21:51:31.
This article is licensed under a Creative Commons Attribution-NonCommercial 3.0 Unported Licence.

high-dimensional representations, through $\mathcal{N}$ iterative iterations using a shared decoder f_{D} with parameters $\xi_{f_{\mathrm{D}}}$:

$$\boldsymbol{S}_{\mathrm{ItR}}^{(k)} = f_{\mathrm{D}}(\boldsymbol{S}_{\mathrm{ItR}}^{(k-1)};\xi_{f_{\mathrm{D}}}),\ k \in \{1,2,3,\ldots,\mathcal{N}\}, \tag{9}$$

where the final compressed image is represented as $\boldsymbol{S}_{\mathrm{ItR}}^{(0)} = \boldsymbol{S}_{\mathrm{ItC}}^{(\mathcal{N})}$, and the spatial dimensions are gradually restored to the original resolution. The shared decoder $f_{\mathrm{D}}: \mathcal{I}_{\mathcal{N}-k+1} \rightarrow \mathcal{I}_{\mathcal{N}-k}$ maps data from a lower resolution level to a higher one. By performing $\mathcal{N}$ iterative reconstruction, the defective image will be reconstructed to their normal state $\boldsymbol{S}_{\mathrm{ItR}}^{(\mathcal{N})}$. Moreover, by successively subtracting the reconstructed normal images $\boldsymbol{S}_{\mathrm{ItR}}^{(k)}$ from the input defective images in the test set $\mathscr{X}_{\mathrm{test}}$, defect maps can be generated:

$$\frac{1}{\mathcal{N}}\sum_{k=1}^{\mathcal{N}}\left(\mathcal{X}_{\mathrm{test}} - S_{\mathrm{ItR}}^{(k)}\right)^2 \Rightarrow \text{defect maps 1.} \tag{10}$$

However, the current defect maps reflect all the defects (dark regions) in the PVEL images, which may not be ideal for industrial detection in specific scenarios. In practice, industrial detection often aims to focus on critical failures, such as significant cracks, fingers and scratch, while ignoring less significant defects. Simply subtracting the reconstructed normal image from the defective image results in the extraction of both true anomalies and background clutter (false positive). To prioritize true defects, multi-image fusion detection is further used, which can selectively emphasize significant anomolies while minimizing the impact of background-induced noise in the final defect maps. The implementation details are provided in the following section.

3.2.3 Multi-image fusion detection. Two sub-tasks are separately conducted in the multi-image fusion detection framework: (1) image fusion using only pseudo masks that simulate structural or visual perturbations, and (2) image fusion incorporating both pseudo masks and functional defect masks (described in Section 2.2). The former enables self-supervised learning by introducing synthetic disruptions to guide feature extraction, while the latter uses a small number of ground-truth (GT)-like functional defect masks to further enhance the model's capability in recognizing real-world PV panel anomalies under a few-shot learning setting.

The reconstructed $\mathcal{N}$ images and the input image (in total $\mathcal{N}+1$ images in each set) are fed into a 3D U-Net (U-Net-Seg), as shown in the red concatenation paths of Fig. 5 and can be expressed as:

$$\mathcal{X}_{\mathrm{test}} \oplus \boldsymbol{S}_{\mathrm{ItR,pseudo}}^{k},\ k \in \{1,2,3,\ldots,\mathcal{N}\} \Rightarrow \text{defect maps 2, and} \tag{11}$$

$$\mathcal{X}_{\mathrm{test}} \oplus (\boldsymbol{S}_{\mathrm{ItR,pseudo}}^{k} + \boldsymbol{S}_{\mathrm{ItR,true}}^{l}),\ k \in \{1,2,3,\ldots,\mathcal{N}\},\ l \in \{1,2,3,\ldots,L\} \Rightarrow \text{defect maps 3} \tag{12}$$

for the sub-tasks 1 and 2, respectively, where L indicates the number of real functional defect mask l. Compared to the conventional 2D network, a 3D U-Net incorporates temporal sequence modeling,[58] allowing the input of $\mathcal{N}$ reconstructed images instead of a single one. This approach enhances structural consistency throughout the reconstruction process. The detailed configurations of pseudo masks and real functional defect masks are provided in Section 4.1.

3.2.4 Theoretical validation of advantages

Enhancement of constraints in function space (advantage 1). The forward pass of the conventional deep AE with N encoder and decoder blocks is given by eqn (3) that $F_{\mathrm{AE}}(\boldsymbol{x}) = f_{\mathrm{D}_1}(f_{\mathrm{D}_2}(\ldots f_{\mathrm{D}_N}(f_{\mathrm{E}_N}(\ldots f_{\mathrm{E}_2}(f_{\mathrm{E}_1}(\boldsymbol{x}))))))$. It shows each encoder block f_{E_i} and decoder block f_{D_i} has its own corresponding parameters $\xi_{f_{\mathrm{E}_i}}$ and $\xi_{f_{\mathrm{D}_i}}$. However, the proposed EI-AE uses a shared encoder f_{E} and a shared decoder f_{D}, each applied $\mathcal{N}$ times:

$$F_{\text{EI-AE}}(\boldsymbol{x}) = f_{\mathrm{D}}^{(k)}(f_{\mathrm{E}}^{(j)}(\boldsymbol{x})) = f_{\mathrm{D}}^{(\mathcal{N})}(f_{\mathrm{D}}^{(\mathcal{N}-1)}(\ldots f_{\mathrm{D}}^{(1)}(f_{\mathrm{E}}^{(\mathcal{N})}(f_{\mathrm{E}}^{(\mathcal{N}-1)}(\ldots f_{\mathrm{E}}^{(1)}(\boldsymbol{x}))))))), \tag{13}$$

$$F_{\text{EI-AE}} \subset F_{\mathrm{AE}}, \tag{14}$$

where the proof is provided in S1.1 of the SI.

In addition, shared parameters $\xi_{f_{\mathrm{E}}}$ and $\xi_{f_{\mathrm{D}}}$ are present in the shared encoder f_{E_i} and decoder f_{D_i}, respectively. Through gradient accumulation during backpropagation, the parameter sharing enforces constraints that ensure scale consistency:

iterative image compression:

$$\frac{\partial F_{\text{EI-AE}}(\boldsymbol{x})}{\partial \xi_{f_{\mathrm{E}}}} = \sum_{j=1}^{\mathcal{N}} \frac{\partial f_{\mathrm{D}}^{(\mathcal{N})}(f_{\mathrm{E}}^{(\mathcal{N})}(\boldsymbol{x}))}{\partial f_{\mathrm{E}}^{(j)}(\boldsymbol{x})} \cdot \frac{\partial f_{\mathrm{E}}^{(j)}(\boldsymbol{x})}{\partial x_{f_{\mathrm{E}}}}, \tag{15}$$

iterative image reconstruction:

$$\frac{\partial F_{\text{EI-AE}}(\boldsymbol{x})}{\partial \xi_{f_{\mathrm{D}}}} = \sum_{k=1}^{\mathcal{N}} \frac{\partial f_{\mathrm{D}}^{(k)}\left(f_{\mathrm{E}}^{(\mathcal{N})}(\boldsymbol{x})\right)}{\partial \xi_{f_{\mathrm{D}}}}. \tag{16}$$

The gradients are computed for all iterations and then combined, guiding the learning process to ensure that the parameters learned by the model remain consistent across all layers. This forces the model to learn representations that are consistent in the function space, thereby avoiding overfitting to any particular scale.

Such analysis demonstrates that the function space in the proposed EI-AE is strictly smaller than that of the conventional AE, further effectively limiting its capacity to memorize arbitrary defect patterns.

Prevention of defect memorization (advantage 2). First, normal and defective image sets are defined as $\mathscr{X}_{\mathrm{norm}}$ and $\mathscr{X}_{\mathrm{anom}}$, respectively. The iterative architecture can be interpreted as utilizing regularization $R(F_{\text{EI-AE}})$ on $\mathscr{X}_{\mathrm{norm}}$ to step-by-step enforce consistency, ensuring stable feature representation across $\mathcal{N}$ iterations:

$$R(F_{\text{EI-AE}}) = \sum_{j=1,k=1}^{\mathcal{N}} \left\| f_D^{(k)}\left(f_E^{(j)}(\boldsymbol{x})\right) - f_D^{(k-1)}\left(f_E^{(j-1)}(\boldsymbol{x})\right) \right\|^2. \tag{17}$$

The expected reconstruction error for defective EL images in the proposed EI-AE, given by the expectation $\mathbb{E}_{\boldsymbol{x}\in\mathscr{X}_{\mathrm{anom}}}$ and bounded below by:

Open Access Article. Published on 26 noiembrie 2025. Downloaded on 13.02.2026 21:51:31.
This article is licensed under a Creative Commons Attribution-NonCommercial 3.0 Unported Licence.

$$\mathbb{E}_{\boldsymbol{x}\in\mathscr{X}_{\text{anom}}}[\|\boldsymbol{x}-f_{\text{D}}^{\mathscr{N}}(f_{\text{E}}^{\mathscr{N}}(\boldsymbol{x};\boldsymbol{x}_{f_{\text{E}}});\boldsymbol{x}_{f_{\text{D}}})\|]\geq c\cdot\min(d(\mathscr{X}_{\text{norm}},\mathscr{X}_{\text{anom}})), \tag{18}$$

where $\min(d(\mathscr{X}_{\text{norm}},\mathscr{X}_{\text{anom}}))$ refers to the minimum distance between normal and defective distributions, and c is a positive constant ($c > 0$) that is a function of the number of iterations $\mathscr{N}$.

This sets a lower bound on the reconstruction error for anomalies, demonstrating that the used iterative architecture effectively prevents memorizing defective patterns without sacrificing the reconstruction of normal data. The detailed explanation is provided in S1.2 of the SI.

Improvement of multi-scale information representation (advantage 3). The iterative architecture with $\mathscr{N}$-step can capture multi-scale information with improved scale consistency. Starting from the iterative reconstruction stage $\boldsymbol{S}_{\text{ItR}}^{(k)}=f_{\text{D}}^{(k)}(f_{\text{E}}^{\mathscr{N}}(\boldsymbol{x}))$, the mutual information $\text{Info}(\cdot;\cdot)$ between $\mathscr{N}$ reconstructions is:

$$\text{Info}(\boldsymbol{S}_{\text{ItR}}^{(k)};\boldsymbol{x})\geq\text{Info}(\boldsymbol{S}_{\text{ItR}}^{(k-1)};\boldsymbol{x}), \tag{19}$$

where the original input $\boldsymbol{x}$ increases monotonically with k. In addition, due to the same iterative operation in each step, the incremental information gain at each step is approximately a constant for normal PVEL images:

$$\frac{\text{Info}(\boldsymbol{S}_{\text{ItR}}^{(k)};\boldsymbol{x}_{\text{norm}})-\text{Info}(\boldsymbol{S}_{\text{ItR}}^{(k-1)};\boldsymbol{x}_{\text{norm}})}{\text{Info}(\boldsymbol{S}_{\text{ItR}}^{(k-1)};\boldsymbol{x}_{\text{norm}})-\text{Info}(\boldsymbol{S}_{\text{ItR}}^{(k-2)};\boldsymbol{x}_{\text{norm}})}\approx\text{const.}, \tag{20}$$

but this consistency breaks down for defective images, hence

$$\frac{\text{Info}(\boldsymbol{S}_{\text{ItR}}^{(k)};x_{\text{anom}})-\text{Info}(\boldsymbol{S}_{\text{ItR}}^{(k-1)};x_{\text{anom}})}{\text{Info}(\boldsymbol{S}_{\text{ItR}}^{(k-1)};x_{\text{anom}})-\text{Info}(\boldsymbol{S}_{\text{ItR}}^{(k-2)};x_{\text{anom}})}\neq\text{const.} \tag{21}$$

Therefore, the proposed EI-AE inherently captures hierarchical information through iterative operation, allowing it to differentiate between normal and defective patterns. A detailed theoretical explanation can be found in S1.3 of the SI.

4 Experimental verification

4.1 Training details

Our network consists of two main components: EI-AE and U-Net-Seg. The EI-AE is responsible for reconstructing a clean version of the input image by eliminating defects, while U-Net-Seg performs pixel-level segmentation to localize defects based on the reconstruction results.

4.1.1 EI-AE (iterative process). The EI-AE is trained using a reconstruction loss defined in eqn (1), which minimizes the ℓ_1 distance between the input image and its reconstructed output. During training, we apply multiple pseudo masks to the input image, each masking a different region to simulate missing or abnormal areas. Despite the masked input, the model is supervised to reconstruct the full, unmasked original image, thereby learning to restore normal content from incomplete or corrupted observations.

4.1.2 U-Net-Seg for multi-image fusion. The U-Net-Seg module is designed to detect defective regions by analyzing reconstruction discrepancies. To construct the input, multiple binary masks are applied to the same input image, simulating various occlusions. Each masked image is independently passed through the EI-AE, resulting in five reconstructed images. These reconstructions are expected to inpaint the masked regions using normal-context priors learned during training. The original masked image, together with the five reconstructions, are concatenated along the channel dimension, forming a 6-channel image. This procedure is repeated for three input instances (*e.g.*, from different views or frames), and their 6-channel representations are concatenated to form a final input tensor of size $18 \times h \times w$, which is interpreted as a 3D volume of size $h \times w \times 18$.

The U-Net-Seg network processes this 3D volume and outputs a single-channel prediction of shape $h \times w \times 1$, which is subsequently flattened to a 2D defect score map. The network is supervised using a pixel-wise ℓ_1 loss between the predicted output and the GT mask, where pixels with value 1 indicate known defective regions. These ground truth masks are derived from the binary masks used for input corruption, guiding the model to focus on regions where the reconstruction deviates from expected normal patterns. In addition, 142 real functional defect masks (1.25% of good images) from the datasets described in Section 2.2 are included to achieve few-shot learning. These real masks will help U-Net-Seg selectively focus on the true defects.

4.1.3 Evalulation metrics. Five different evaluation metrics are used for assessing pixel-wise defect detection performance, comprising (i) three pixel-level metrics: pixel-wise area under the receiver operating characteristic curve (P-AUROC),[59] pixel-wise average precision (P-AP),[60] and pixel-wise F1 score (P-F1)[60]; (ii) two regional-level metrics: area under the per-region overlap curve (AUPRO),[61] and area per-region overlap (A-PRO).[61]

P-AUROC measures the model's ability to distinguish between normal and defective pixels across all threshold values. P-AP is calculated as the area under the precision–recall (PR) curve, reflecting the trade-off between precision and recall. P-F1 is defined as the harmonic mean of precision and recall at the optimal threshold, providing a single-value summary of detection accuracy.

AUPRO evaluates detection performance across varying false positive rates by measuring how well predicted regions cover ground-truth defects. A-PRO calculates the proportion of ground-truth regions correctly detected, considering a prediction successful if the intersection over union (IoU) exceeds a predefined threshold (0.3 in this study).

4.2 Experiment 1 – unsupervised detection of all defects (No U-Net-Seg)

4.2.1 Overall performance comparison. Based on eqn (10), the proposed EI-AE performs segmentation of all defects under the unconditional defect detection scenario (corresponding to defect Maps 1 in Fig. 5). This enables direct pixel-level localization of defects that all defects are treated uniformly as defects, without imposing specific conditional constraints. In addition to the proposed EI-AE, four classic segmentation networks (AE,[52] EdgeRec,[62] DRAEM,[63] and U-Net[49]) are trained to

Open Access Article. Published on 26 noiembrie 2025. Downloaded on 13.02.2026 21:51:31.
This article is licensed under a Creative Commons Attribution-NonCommercial 3.0 Unported Licence.

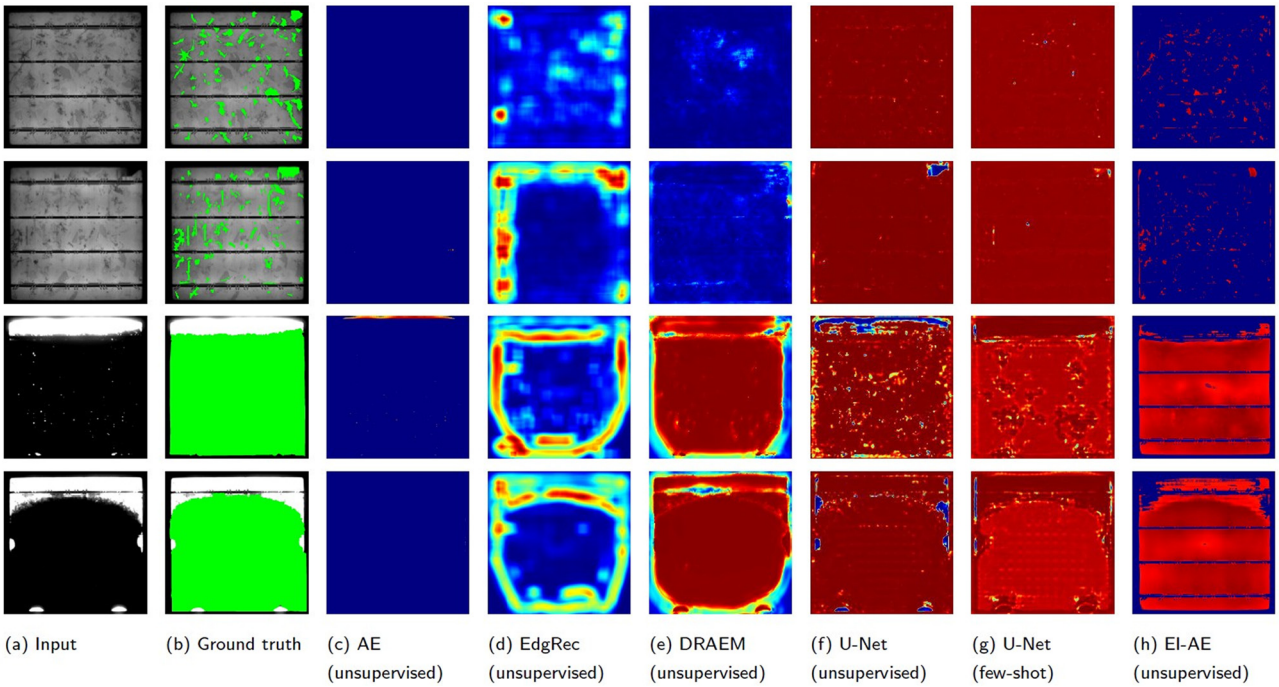

Fig. 6 Segmentation results of all defects using unsupervised defect detection (Experiment 1).

demonstrate the superiority of EI-AE in fully unsupervised defect segmentation of PVEL images. It should be mentioned that AE, EdgRec, and DREAM are classic unsupervised segmentation networks that operate without any labelled data, whereas U-Net requires either pseudo labels or true labels (142 images from Mask B – Section 2.2) to perform segmentation.

Fig. 6 (segmentation maps) and Table 1 (metrics) illustrate the comparison results, obtained by directly computing pixel-wise differences between the reconstructed images and their original counterparts. For performance evaluation, the GT is defined using the full defect masks (Mask A) as described in Section 2.1. Although EI-AE achieves slightly lower P-AP (0.6434) and P-F1 (0.6739) compared to DRAEM (0.7248 and 0.7206 respectively), it consistently outperforms all baseline methods in the remaining three metrics: P-AUROC (0.8800), AUPRO (0.4074), and A-PRO (0.8557). These results indicate that EI-AE provides stronger global discrimination capability and better robustness in identifying true functional defects across diverse pixel regions, while DRAEM tends to focus more on pixel-level differences, which may lead to higher precision in localized areas but lower overall consistency and generalization performance. The performance of the conventional AE is poorest because the model tends to take a shortcut during reconstruction by simply copying the input to the output. As a result, it also learns to reconstruct the defects, making it difficult to distinguish them from normal regions [eqn (5) and (6)]. In general, the results demonstrate the strong generalization capability of the proposed EI-AE in scenarios that demand comprehensive detection of diverse defect types in PVEL images.

Table 1 Comparison of pixel-level metrics across different methods in Experiment 1

Methods	P-AUROC	P-AP	P-F1	AUPRO	A-PRO
AE (unsupervised)	0.5772	0.2002	0.3757	0.0239	0.0212
EdgRec (unsupervised)	0.5448	0.2687	0.3099	0.1515	0.4060
DRAEM (unsupervised)	0.8596	0.7248	0.7206	0.1251	0.8202
U-Net (unsupervised)	0.5349	0.2449	0.3096	0.1232	0.3104
U-Net (few-shot)[a]	0.7571	0.5379	0.6207	0.1625	0.6939
EI-AE (unsupervised)	0.8800	0.6434	0.6739	0.4074	0.8557

[a] U-Net is trained with functional defect masks (Mask B) to enable few-shot segmentation.

4.2.2 Incremental reconstruction performance of proposed EI-AE. Since the proposed EI-AE relies on iterative operations to progressively capture fine-grained defect details in PVEL images, restore anomaly images to their normal counterparts, and subsequently obtain anomaly segmentation, it is essential to validate its incremental reconstruction performance. Fig. 7 (four images with highly severe defects) visually illustrates the enhancement in reconstruction quality across five iterative stages, effectively demonstrating the model's ability to gradually capture and restore complex details. Defects within the data are incrementally diminished through successive reconstruction steps, highlighting the model's proficiency in identifying and progressively mitigating defective features.

Notably, the maximum feasible compression depth is $\mathcal{N} = 5$, as it represents the limit imposed by the 1024 × 1024 input resolution and the downsampling factor of two per stage. Beyond this depth, the feature maps shrink to sizes below 32 × 32, potentially resulting in loss of spatial context, misalignment in the decoder, and numerical instability due to over-compression.

Open Access Article. Published on 26 noiembrie 2025. Downloaded on 13.02.2026 21:51:31.
This article is licensed under a Creative Commons Attribution-NonCommercial 3.0 Unported Licence.

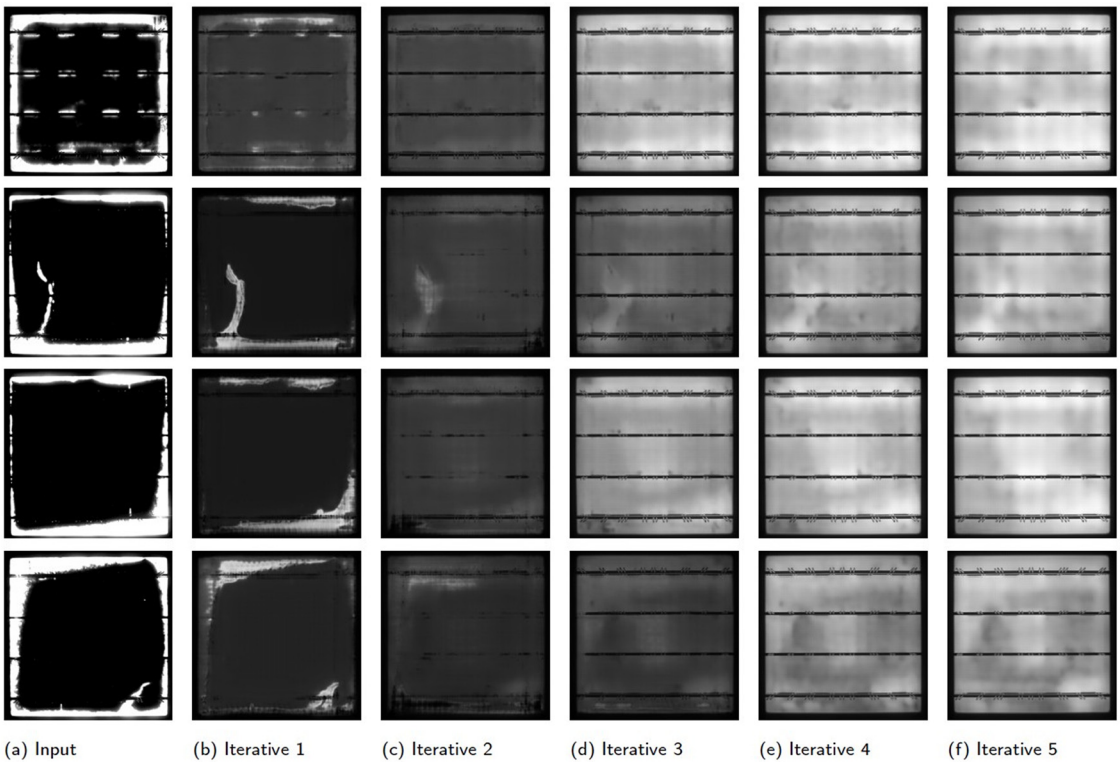

Fig. 7 Step-by-step reconstruction (iterative 1 to iterative 5) in the proposed EI-AE.

4.3 Experiment 2 – unsupervised defect detection using U-Net-Seg

By incorporating a segmentation head (referred to the multi-image fusion module, U-Net-Seg) and introducing annotated defect masks, the proposed EI-AE model is able to detect more specific defects in PVEL images. The test images are selected from the "Crack (non-star)" category in Mask B, as shown in Fig. 4(a), for evaluating the performance of all networks.

Fig. 8 presents the segmentation results obtained by fusing the input image with five piecewise recovery images as input to U-Net-Seg, where only pseudo masks are used during training [eqn (11)]. Table 2 presents the quantitative comparison of different unsupervised methods for the "Crack (non-star)" category. The proposed EI-AE achieves the best overall performance, with the highest scores in P-AUROC (0.8868), AUPRO (0.6297), and A-PRO (0.8814), indicating superior pixel-wise discrimination and region-level defect localization. While P-AP (0.1428) and P-F1 (0.2076) are slightly lower than those of the U-Net baseline (0.2503 and 0.3355, respectively), EI-AE maintains a better balance across all metrics. This suggests that EI-AE avoids overfitting to local noise and generalizes better in complex surface defect scenarios. Although the integration of U-Net-Seg in the conventional AE significantly improves its performance, it still falls short of EI-AE, confirming the critical role of the embedded iterative operation in enhancing defect localization and suppression of irrelevant features.

4.4 Experiment 3 – few-shot defect detection using U-Net-Seg

In the third experiment, true masks (functional defect masks – Mask B) are also included in the training process of the proposed EI-AE, in addition to the pseudo masks. A total of 142 real functional defect masks are randomly selected from the category groups of finger interruptions, scratches, and star cracks, while the non-star crack category group is used to evaluate the network performance.

Despite comprising only 1.25% of the good images, the inclusion of true masks contributes to improved prediction accuracy and more precise defect segmentation with reduced background interference [Fig. 9(e)], as demonstrated in the comparison of EI-AE results in Experiment 2 [Fig. 8(h)]. An accuracy improvement of 3.04% is achieved in the few-shot setting (P-AUROC: 0.9138), compared to the baseline without few-shot learning (P-AUROC: 0.8868).

Table 3 compares the performance of AE, U-Net, and the proposed EI-AE in a few-shot defect segmentation setting. In terms of P-AUROC, EI-AE achieves the highest score of 0.9138, outperforming AE (0.8586) and U-Net (0.7923), indicating improved defect segmentation at the pixel level. For P-AP, EI-AE reaches 0.3425, which remains higher than that of U-Net (0.2870) and noticeably better than that of AE (0.2098), suggesting better precision–recall trade-off. The P-F1 of EI-AE is 0.4208, significantly higher than that of AE (0.3054) and slightly higher than that of U-Net (0.4205), reflecting more accurate segmentation boundaries. In terms of region-aware metrics, EI-AE also demonstrates competitive performance, achieving an AUPRO of 0.7576, slightly lower than that of AE (0.7916) but significantly higher than that of U-Net (0.5446). Similarly, the region-wise A-PRO of EI-AE reaches 0.8185, exceeding that of U-Net (0.6852) and only marginally lower than that of AE (0.8193). These

 This journal is © The Royal Society of Chemistry 2026

Open Access Article. Published on 26 noiembrie 2025. Downloaded on 13.02.2026 21:51:31.
This article is licensed under a Creative Commons Attribution-NonCommercial 3.0 Unported Licence.

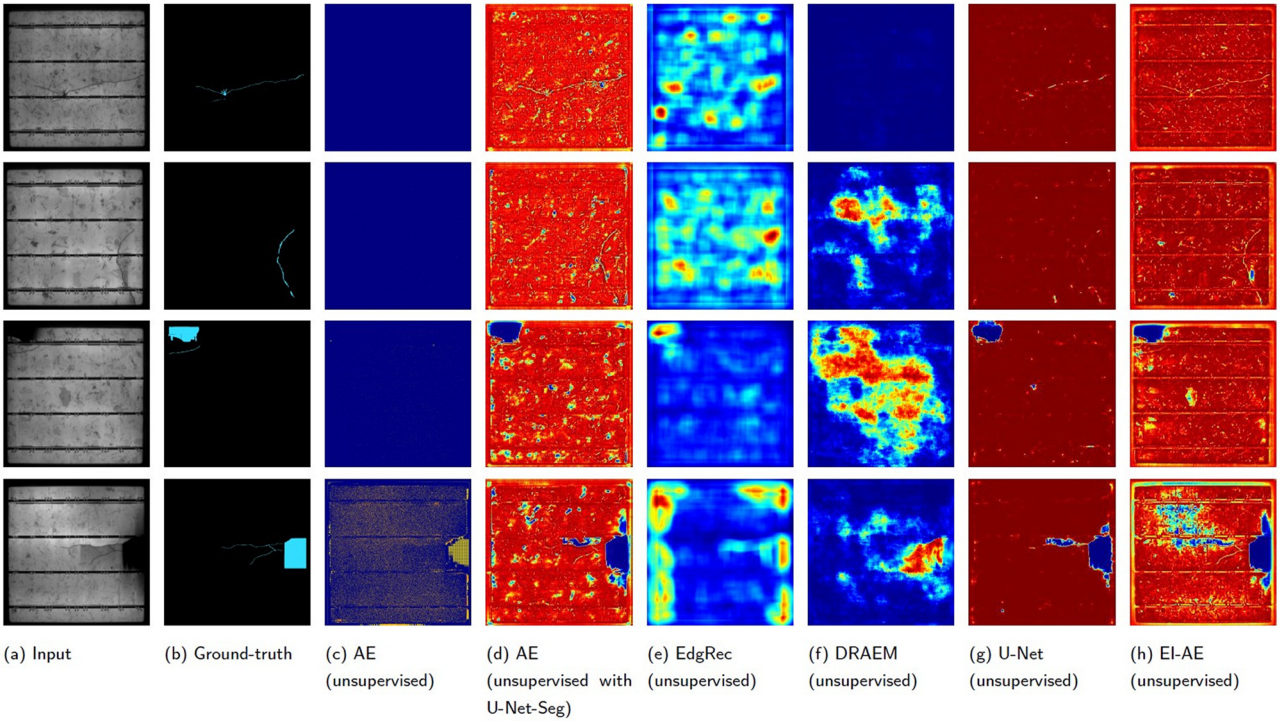

Fig. 8 Segmentation results using unsupervised defect detection (Experiment 2).

Table 2 Comparison of pixel-level metrics across different methods in Experiment 2

Methods	P-AUROC	P-AP	P-F1	AUPRO	A-PRO
AE (unsupervised)	0.5108	0.0034	0.0074	0.5508	0.1512
AE (unsupervised with U-Net-Seg)[a]	0.8135	0.0651	0.1659	0.5508	0.7641
EdgRec (unsupervised)	0.6175	0.0068	0.0226	0.2534	0.4635
DRAEM (unsupervised)	0.6666	0.0491	0.1110	0.3368	0.5676
U-Net (unsupervised)	0.7353	0.2503	0.3355	0.4226	0.4985
EI-AE (unsupervised)[a]	0.8868	0.1428	0.2076	0.6297	0.8814

[a] Segmentation head (U-Net-Seg) is included in the conventional AE and the proposed EI-AE.

results confirm the effectiveness of the enhanced iterative structure in improving segmentation accuracy and robustness with limited supervision.

To further illustrate how accuracy varies with different sampling sizes in the few-shot setting, we conduct an additional experiment testing 1-, 10-, and 50-shot scenarios, respectively. As shown in Table 4, the 1-shot case performs worse than the unsupervised one (0.8868) because a single labelled sample provides insufficient and potentially misleading supervision, disrupting the model's originally stable feature representation. However, as the number of shots increases, the accuracy improves rapidly and approaches saturation at 50-shot, demonstrating the model's strong few-shot learning capability.

5 Implications and challenges in real-world manufacturing

The spatial distribution and trends of defects detected by the proposed EI-AE can be correlated with specific PV panel manufacturing steps (*e.g.*, wafer cutting, cell soldering, encapsulation, lamination, or module assembly), serving as an effective quality control tool across various production stages. Moreover, the obtained defect maps can be integrated with statistical process control or optimization frameworks to quantitatively assess the impact of manufacturing parameters, enabling engineers to identify critical process stages and proactively guide process improvements.

There are also some major challenges in practical deployment. First, building a larger set of high-quality PV-EL defect-free and defective images remains a challenge, especially for emerging PV materials such as perovskite and CIGS. Secondly, the current implementation does not explicitly distinguish defect types; integrating a dedicated classifier model would be a promising yet non-trivial step toward enabling automatic defect categorization. Lastly, in real production lines where PV panels may exhibit variations in shape, orientation, and layout, developing a model robust to such variations is still an open challenge. The proposed EI-AE paves the way for the

Open Access Article. Published on 26 noiembrie 2025. Downloaded on 13.02.2026 21:51:31.
This article is licensed under a Creative Commons Attribution-NonCommercial 3.0 Unported Licence.

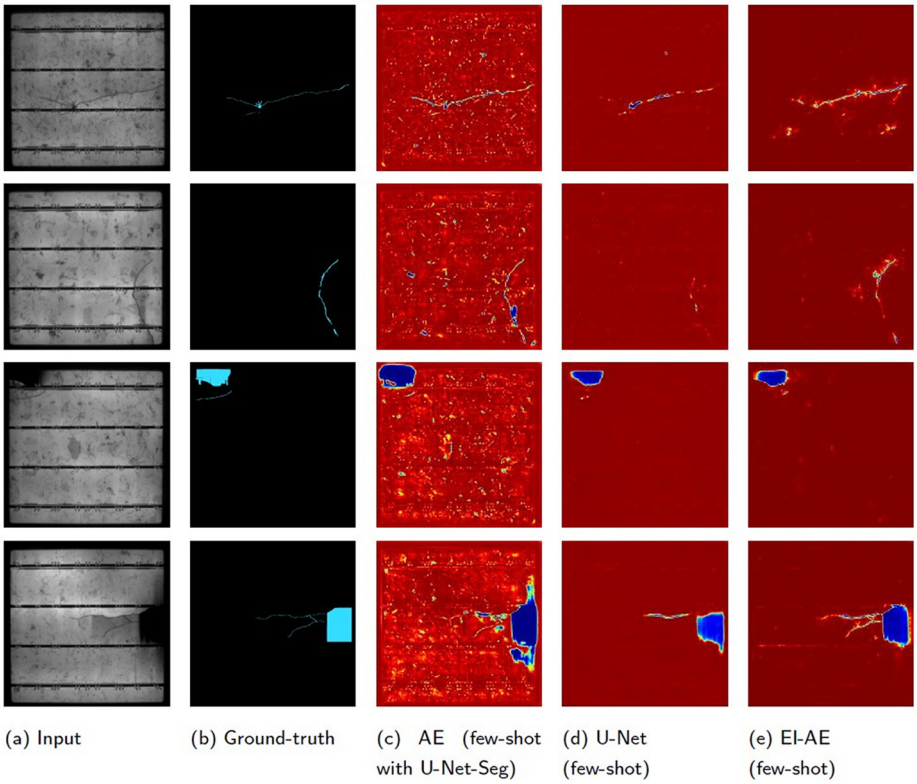

Fig. 9 Segmentation results of using few-shot defect detection (Experiment 3).

Table 3 Comparison of pixel-level metrics across different methods in Experiment 3

Methods	P-AUROC	P-AP	P-F1	AUPRO	A-PRO
AE (few-shot with U-Net-Seg)[a]	0.8586	0.2098	0.3054	0.7916	0.8193
U-Net (few-shot)	0.7923	0.2870	0.4205	0.5446	0.6852
EI-AE (few-shot)[a]	0.9138	0.3425	0.4208	0.7576	0.8185

[a] Segmentation head (U-Net-Seg) is included in the conventional AE and the proposed EI-AE.

Table 4 Comparison of pixel-level AUROC of proposed EI-AE under different few-shot scenarios in Experiment 3

Methods	EI-AE (1-shot) (%)	EI-AE (10-shot) (%)	EI-AE (50-shot) (%)	EI-AE (142-shot) (%)
P-AUROC	74.5	88.6	91.5	91.4

development of more robust and adaptive models capable of handling these practical complexities.

6 Conclusion

Given that current PVEL anomaly detection methods predominantly apply classical segmentation networks with limited adaptability to subtle or complex defects, this study proposes a novel EI-AE framework to achieve more precise defect segmentation of complex anomalies in PV modules. Instead of relying on implementation-complex architectures, a simple yet effective iterative structure is adopted, introducing a small number of iterative steps within each encoder and decoder block to support effective deep feature extraction. Moreover, the proposed multi-image fusion structure concatenates the original inputs with all recovered images generated during the iterative process, achieving more precise segmentation of specific anomalies in PVEL images while using only a limited number of real labels.

Three experiments, including (1) unsupervised detection of all defects, (2) unsupervised detection with segmentation head, and (3) few-shot detection with segmentation head, progressively demonstrate the superior performance of the proposed EI-AE over conventional methods. The proposed EI-AE reduces the need for extensive labelled data, making it highly suitable for large-scale PV module inspection in industrial settings. Its simple design and adaptability to complex defects also support efficient deployment in real-world manufacturing and maintenance scenarios.

Author contributions

Ye Lin: conceptualization, data curation, investigation, methodology, writing – original draft; Pingyang Sun: conceptualization, formal analysis, investigation, methodology, visualization,

 This journal is © The Royal Society of Chemistry 2026

Open Access Article. Published on 26 noiembrie 2025. Downloaded on 13.02.2026 21:51:31.
This article is licensed under a Creative Commons Attribution-NonCommercial 3.0 Unported Licence.

writing – original draft; Rongcheng Wu: conceptualization, data curation, methodology, software, validation, writing – original draft; Shu Geng: investigation, visualization, writing – review & editing; Man Lung Yiu: methodology, supervision, writing – review & editing; Zhidong Li: methodology, project administration, supervision; Fang Chen: project administration, supervision; Yu Gao: project administration, supervision; Mingzhe Wang: project administration, supervision, writing – review & editing; Kaiwen Sun: supervision, writing – review & editing; Xiaojing Hao: supervision, writing – review & editing.

Conflicts of interest

The authors declare no conflicts of interest.

Data availability

The data supporting this article have been included as part of the supplementary information (SI). Supplementary information: the Photovoltaic Electroluminescence Anomaly Detection (PVEL-AD) dataset is used in this article: su binyi, Photovoltaic cell anomaly detection, https://kaggle.com/competitions/pvelad, 2022, Kaggle. In addition, the annotated masks in this paper have been included. Codes of the proposed EI-AE will be made publicly available on GitHub in the final version, https://github.com/rongcheng-wu/Abnormal-detection-in-Photovoltaic-Electroluminescence-Images. See DOI: https://doi.org/10.1039/d5ee05042a.

Acknowledgements

This work is supported by the Australia – UK Renewable Hydrogen Innovation Partnerships (GA396723), funded by the Department of Climate Change, Energy, the Environment and Water, Australian Government. This work is also partly supported by the National Natural Science Foundation of China (No. 62306223), the China Postdoctoral Science Foundation (No. 2024M752533), the Young Talent Fund of Xi'an Association for Science and Technology (No. 959202413053), the Fundamental Research Funds for the Central Universities (No. XJSJ24020), and the Xiaomi Young Talents Program.

References

1 T. Fuyuki, H. Kondo, T. Yamazaki, Y. Takahashi and Y. Uraoka, *Appl. Phys. Lett.*, 2005, **86**, 262108.
2 M. Köntges, S. Kurtz, C. E. Packard, U. Jahn, K. A. Berger, K. Kato, T. Friesen, H. Liu, M. Van Iseghem, J. Wohlgemuth, *et al.*, Review of failures of photovoltaic modules, IEA International Energy Agency, https://iea-pvps.org/wp-content/uploads/2020/01/IEA-PVPS_T13-01_2014_Review_of_Failures_of_Photovoltaic_Modules_Final.pdf, 2014.
3 G. Pang, C. Shen, L. Cao and A. V. D. Hengel, *ACM Comput. Surv.*, 2021, **54**, 1–38.
4 B. Su, Z. Zhou and H. Chen, *IEEE Trans. Industr. Inform.*, 2023, **19**, 404–413.
5 B. Su, H. Chen, P. Chen, G. Bian, K. Liu and W. Liu, *IEEE Trans. Industr. Inform.*, 2021, **17**, 4084–4095.
6 S. Spataru, P. Hacke and D. Sera, 2016 IEEE 43rd Photovoltaic Specialists Conference (PVSC), 2016, pp. 1602–1607.
7 H. Chen, H. Zhao, D. Han and K. Liu, *Opt. Lasers Eng.*, 2019, **118**, 22–33.
8 J. Balzategui, L. Eciolaza, N. Arana-Arexolaleiba, J. Altube, J.-P. Aguerre, I. Legarda-Ereno and A. Apraiz, 2019 24th IEEE International Conference on Emerging Technologies and Factory Automation (ETFA), 2019, pp. 529–535.
9 H. Munawer Al-Otum, *Sol. Energy*, 2024, **278**, 112803.
10 F. Demir, *IEEE Access*, 2025, **13**, 58481–58495.
11 A. Bartler, L. Mauch, B. Yang, M. Reuter and L. Stoicescu, 2018 26th European Signal Processing Conference (EUSIPCO), 2018, pp. 2035–2039.
12 H. Yousif and Z. Al-Milaji, *Sol. Energy*, 2024, **267**, 112207.
13 J. Zhang, X. Chen, H. Wei and K. Zhang, *Appl. Energy*, 2024, **355**, 122184.
14 J. Wu, E. Chan, R. Yadav, H. Gopalakrishna and G. TamizhMani, *New Concepts in Solar and Thermal Radiation Conversion and Reliability*, 2018, p. 1075915.
15 M. Dhimish and Y. Hu, *Sci. Rep.*, 2022, **12**, 12168.
16 D.-M. Tsai and J.-Y. Luo, *IEEE Trans. Industr. Inform.*, 2011, **7**, 125–135.
17 Y. Li, C. He, Y. Lyu, G. Song and B. Wu, *NDT&E Int.*, 2019, **102**, 129–136.
18 C. Mantel, S. Spataru, H. Parikh, D. Sera, G. A. D. R. Benatto, N. Riedel, S. Thorsteinsson, P. B. Poulsen and S. Forchhammer, 2018 IEEE 7th World Conference on Photovoltaic Energy Conversion (WCPEC) (A Joint Conference of 45th IEEE PVSC, 28th PVSEC & 34th EU PVSEC), 2018, pp. 0433–0437.
19 E. Sovetkin and A. Steland, *Integr. Comput.-Aided Eng.*, 2019, **26**, 123–137.
20 M. Sun, S. Lv, X. Zhao, R. Li, W. Zhang and X. Zhang, *Defect Detection of Photovoltaic Modules Based on Convolutional Neural Network*, Springer International Publishing, 2018, pp. 122–132.
21 X. Zhang, Y. Hao, H. Shangguan, P. Zhang and A. Wang, *Infrared Phys. Technol.*, 2020, **108**, 103334.
22 M. Mayr, M. Hoffmann, A. Maier and V. Christlein, 2019 IEEE International Conference on Image Processing (ICIP), 2019.
23 Y. Guo, Y. Liu, T. Georgiou and M. S. Lew, *Int. J. multimed. Inf. Retr.*, 2018, **7**, 87–93.
24 X. Zhao, C. Song, H. Zhang, X. Sun and J. Zhao, *Energy*, 2023, **267**, 126605.
25 J. Wang, L. Bi, P. Sun, X. Jiao, X. Ma, X. Lei and Y. Luo, *Sensors*, 2022, **23**, 297.
26 A. Ahmad, Y. Jin, C. Zhu, I. Javed, A. Maqsood and M. W. Akram, *IET Renew. Power Gen.*, 2020, **14**, 2693–2702.
27 A. M. Karimi, J. S. Fada, J. Liu, J. L. Braid, M. Koyuturk and R. H. French, 2018 IEEE 7th World Conference on Photovoltaic Energy Conversion (WCPEC) (A Joint Conference of

Open Access Article. Published on 26 noiembrie 2025. Downloaded on 13.02.2026 21:51:31.
This article is licensed under a Creative Commons Attribution-NonCommercial 3.0 Unported Licence.

45th IEEE PVSC, 28th PVSEC & 34th EU PVSEC), 2018, pp. 0418–0424.
28 S. Deitsch, V. Christlein, S. Berger, C. Buerhop-Lutz, A. Maier, F. Gallwitz and C. Riess, *Sol. Energy*, 2019, **185**, 455–468.
29 M. Demirci, N. Besli and A. Gümüşçü, Defective PV Cell *Detection Using Deep Transfer Learning and EL Imaging*, *International Conference on Data Science, Machine Learning and Statistics - 2019 (DMS-2019)*, Van Yuzuncu Yil University, 2019.
30 A. M. Karimi, J. S. Fada, M. A. Hossain, S. Yang, T. J. Peshek, J. L. Braid and R. H. French, *IEEE J. Photovolt.*, 2019, **9**, 1324–1335.
31 W. Tang, Q. Yang and W. Yan, 2019 IEEE PES Asia-Pacific Power and Energy Engineering Conference (APPEEC), 2019, pp. 1–5.
32 W. Tang, Q. Yang, K. Xiong and W. Yan, *Sol. Energy*, 2020, **201**, 453–460.
33 M. Y. Demirci, N. Beşli and A. Gümüşçü, *Expert Syst. Appl.*, 2021, **175**, 114810.
34 C. Ge, Z. Liu, L. Fang, H. Ling, A. Zhang and C. Yin, *IEEE Trans. Parallel Distrib. Syst.*, 2021, **32**, 1653–1664.
35 C. Huang, Z. Zhang and L. Wang, *IEEE J. Photovolt.*, 2022, **12**, 1550–1558.
36 X. Chen, T. Karin and A. Jain, *Sol. Energy*, 2022, **242**, 20–29.
37 C. Mantel, F. Villebro, G. Alves Dos Reis Benatto, H. Rajesh Parikh, S. Wendlandt, K. Hossain, P. B. Poulsen, S. Spataru, D. Séra and S. Forchhammer, *Appl. Mach. Learn.*, 2019, 1.
38 Y. Zhao, K. Zhan, Z. Wang and W. Shen, *Prog. Photovoltaics Res. Appl.*, 2021, **29**, 471–484.
39 U. Otamendi, I. Martinez, M. Quartulli, I. G. Olaizola, E. Viles and W. Cambarau, *Sol. Energy*, 2021, **220**, 914–926.
40 A. Korovin, A. Vasilyev, F. Egorov, D. Saykin, E. Terukov, I. Shakhray, L. Zhukov and S. Budennyy, *arXiv*, 2022, preprint, arXiv:2208.05994, DOI: 10.48550/arXiv.2208.05994.
41 J. Fioresi, D. J. Colvin, R. Frota, R. Gupta, M. Li, H. P. Seigneur, S. Vyas, S. Oliveira, M. Shah and K. O. Davis, *IEEE J. Photovolt.*, 2022, **12**, 53–61.
42 C. Shou, L. Hong, W. Ding, Q. Shen, W. Zhou, Y. Jiang and C. Zhao, 2020 35th Youth Academic Annual Conference of Chinese Association of Automation (YAC), 2020, pp. 312–317.
43 M. R. U. Rahman and H. Chen, *IEEE Access*, 2020, **8**, 40547–40558.
44 L. Pratt, D. Govender and R. Klein, *Renewable Energy*, 2021, **178**, 1211–1222.
45 E. Sovetkin, E. J. Achterberg, T. Weber and B. E. Pieters, *IEEE J. Photovolt.*, 2021, **11**, 444–452.
46 L. Pratt, J. Mattheus and R. Klein, *Syst. Soft Comput.*, 2023, **5**, 200048.
47 B. Yang, Z. Zhang and J. Ma, *IEEE Sens. J.*, 2025, **25**, 891–903.
48 R. Duan, Y. Wang, X. Chen and S. Li, *Energy*, 2025, **331**, 136711.
49 O. Ronneberger, P. Fischer and T. Brox, in *U-Net: Convolutional Networks for Biomedical Image Segmentation*, Springer International Publishing, 2015, pp. 234–241.
50 M. Burgin, *Super-recursive algorithms*, Springer Science & Business Media, 2006.
51 su binyi, Photovoltaic cell anomaly detection, https://kaggle.com/competitions/pvelad, 2022, Kaggle.
52 D. Gong, L. Liu, V. Le, B. Saha, M. R. Mansour, S. Venkatesh and A. v d Hengel, *IEEE Int. Conf. Comput. Vis. Workshops*, 2019, 1705–1714.
53 P. Bergmann, K. Batzner, M. Fauser, D. Sattlegger and C. Steger, *Int. J. Conf. Violence*, 2022, **130**, 947–969.
54 D. P. Kingma and M. Welling, *et al.*, *Foundations and Trends in Machine Learning*, 2019, vol. 12, pp. 307–392.
55 P. Bergmann, S. Löwe, M. Fauser, D. Sattlegger and C. Steger, *arXiv*, 2018, preprint, arXiv:1807.02011, DOI: 10.48550/arXiv.1807.02011.
56 V. Zavrtanik, M. Kristan and D. Skocaj, *Int. J. Conf. Violence*, 2021, 8330–8339.
57 N.-C. Ristea, N. Madan, R. T. Ionescu, K. Nasrollahi, F. S. Khan, T. B. Moeslund and M. Shah, *CVPR*, 2022, 13576–13586.
58 S. Ji, W. Xu, M. Yang and K. Yu, *IEEE Trans. Pattern Anal. Mach. Intell.*, 2012, **35**, 221–231.
59 J. A. Hanley and B. J. McNeil, *Radiology*, 1983, **148**, 839–843.
60 P. Bergmann, M. Fauser, D. Sattlegger and C. Steger, Proceedings of the IEEE/CVF conference on computer vision and pattern recognition, 2019, pp. 9592–9600.
61 K. Roth, L. Pemula, J. Zepeda, B. Schölkopf, T. Brox and P. Gehler, Proceedings of the IEEE/CVF conference on computer vision and pattern recognition, 2022, pp. 14318–14328.
62 T. Liu, B. Li, Z. Zhao, X. Du, B. Jiang and L. Geng, *arXiv*, 2022, preprint, arXiv:2210.14485, DOI: 10.48550/arXiv.2210.14485.
63 V. Zavrtanik, M. Kristan and D. Skočaj, Proceedings of the IEEE/CVF international conference on computer vision, 2021, pp. 8330–8339.

 This journal is © The Royal Society of Chemistry 2026